Vietnam Journal of Earth Sciences, 45(2), 251-270, https://doi.org/10.15625/2615-9783/18407

Vietnam Journal of Earth Sciences
https://vjs.ac.vn/index.php/jse

Coastline and shoreline change assessment in sandy coasts based on machine learning models and high-resolution satellite images

Tuan Linh Giang[1,2*], Kinh Bac Dang[1], Quang Thanh Bui[1]

[1] *VNU University of Science, Vietnam National University, Hanoi, 10000, Vietnam*
[2] *VNU Institute of Vietnamese Studies and Development Science (VNU-IVIDES), Vietnam National University, Hanoi, 10000, Vietnam*

Received 26 December 2022; Received in revised form 23 April 2023; Accepted 31 May 2023

ABSTRACT

Changes to the coastline or shoreline arise from the water's dynamic interaction with the land surface, which is triggered by ocean currents, waves, and winds. Various methods have been proposed to identify and monitor coastlines and shorelines, but their outcomes are uncertain. This study proposes indicators for identifying coastlines and shorelines in the fields and on the remote sensing data. Different pixel- and object-based machine learning (ML) models were built to automatically interpret coastlines and shorelines from high-resolution remote sensing images and monitor coastal erosion in Vietnam. Two pixel-based models using Random Forest and SVM structures and eight object-based models using U-Net, and U-Net3+ structures were trained. All models were trained using the high-resolution images gathered using Google Earth Pro as input data. The U-Net achieves the most remarkable performance of 98% with a loss function of 0.16 when utilizing an input-image size of 512×512.

Object-based models have shown higher performance in analyzing coastlines and shorelines with linear and continuous structures than pixel-based models. Additionally, the coastline is appropriate to evaluate coastal erosion induced by the effect of sea-level rise during storms. At the same time, the shoreline is suited to observe seasonal tidal fluctuations or the instantaneous movements of current waves. Under the pressure of tourist development, the coasts in Danang and Quang Nam provinces have been eroded in the last 10 years. River and ocean currents also cause erosion in the southern Cua Dai estuary. In the future, the trained U-Net model can be used to monitor the changes in coastlines and shorelines worldwide.

Keywords: Erosion; Unet; Support Vector Machine; Random Forest; Google Earth.

1. Introduction

Ocean currents, waves, and winds complicate the interaction of sea and land surfaces, leading to shoreline changes (Martínez et al., 2018; Nazeer et al., 2020). 70% of loose-material-containment beaches worldwide have seen catastrophic erosion in the past 30 years (Dang et al., 2022a; Escudero-Castillo et al., 2018). Since 1970, various American eroded coasts have averaged 0.6 to 0.9 m/year, with the east coast averaging 2.6 to 3.1 m/year (Titus and Richman, 2001). Many countries with long coasts have made efforts to monitor shoreline

---

*Corresponding author, Email: gianglinh1031@gmail.com erosion (Gallina et al., 2020; Hanley et al., 2014; Martínez et al., 2018). Europe's coastal erosion affects the likelihood of people on the almost 20,000 km coastline (Hanley et al., 2014; Mineur et al., 2015). All information now has not been updated and depends strongly on expert knowledge. To track shoreline and coastline changes, managers should be equipped with artificial intelligence tools to track coastal erosion and sea-level rise. The outcome information from these tools must be updated quickly and correctly to inform people in time about the future coastal parts that will be eroded.

Remote sensing technology provides multi-sensor, multi-temporal, and high-resolution data for machine learning (ML) models (Dang et al., 2020b; Gordana and Avdan, 2019; Nirmala et al., 2022). Remote sensing (RS) and geographic information systems (GIS) have been utilized in coastal erosion studies to offer management recommendations (Dang et al., 2022c; Hoang et al., 2022). Since the scientific understanding of coastline/shoreline markers differs, predictions related to coastal erosion contain uncertainties (Pollard et al., 2020; Toure et al., 2019). Input image data sources and processing software significantly affect outcome interpretation. In past studies examining the process of coastal erosion, mid-resolution satellite images (like Landsat, SPOT, and Sentinel-2) were commonly used to segregate land from the ocean in general (Loi et al., 2021). The Sentinel-2 sensor provides images with the highest accuracy of 10m in the free middle satellite image data. However, the distance between the coastline and the shoreline is only about 5 to 10m. Therefore, using middle satellite images to detect coastal erosion is ineffective. Nowadays, many other remote sensing devices, such as unmanned aerial vehicles (UAV) and Google Earth photos with resolutions of up to 0.3 m to 1 m, may be employed to analyze coastlines and shorelines to tackle this issue (Dang et al., 2022a; Vu et al., 2004). It can help accurately locate and date shorelines and coastlines in real-time. However, Landsat and Sentinel missions have been the most extensively utilized sources of remote sensing data, while very high-resolution images account for a small part.

Recently, ArcGIS, ENVI 5.1, eCognition, and DSAS software have been used to examine the shoreline's and coastline's changes (Loi et al., 2021). However, these methods cannot analyze large amounts of data or develop AI models (Tran and Prakash, 2020). Meanwhile, experts still interpret coastlines and shorelines, especially with high-resolution images. Based on the development of ML technology, developers may train computers to separate coastlines and shorelines from neighboring coastal objects (Dang et al., 2022a). Accordingly, the computer can distinguish the shoreline and coastline during remote sensing image analysis, creating real-time coastal change monitoring models. Different ML structures, such as SVM, CNN, Unet, U2Net, Unet3+, and DexiNed, have been used in geology (Hoang et al., 2021; Nguyen et al., 2022a; Nhu et al., 2022; T. B. Pham et al., 2022), hydrology (Duong et al., 2022; T. A. Nguyen et al., 2020), lithology (Le et al., 2020; Pham et al., 2020), and the environmental fields (D. T. Nguyen et al., 2020; Nirmala et al., 2022). The application of these models has not been tested with the task of identifying coastlines, shorelines, and coastal erosion.

To accurately locate shorelines and coastlines supporting coastal erosion analysis in the field and on high-resolution satellite images, this research attempts to: (1) propose an indicator system; (2) compare ML models using pixel- and object-based approaches in automatically defining shorelines and coastlines from high-resolution remote sensing data; and (3) use these models to assess coastal erosion in the Center path of Vietnam. The categorization of the coastline and shorelines was investigated in this research using several ML models built from the random forest (RF), support vector machine (SVM), and different artificial neural networks (presented in sections 2.2 and 2.3). The findings of this work may be used to provide a method for using an ML model for tracking erosion along various coastline types in Vietnam and elsewhere in the globe.

2. Material and methods

2.1. Machine learning structures for coastline/shoreline classification

The classification of coasts and shorelines was broken down into three primary phases, as indicated in Fig. 1. Step 1 was completed both inside the lab and outside through field investigation to determine the appropriate coastline and shoreline criteria for each coastal type. To produce sample data from remote sensing images, ground truth points (GTP) were found on the fields and processed with Google Earth images. Step 2 involves the categorization of coastlines and shorelines using pixel- and object-based ML models. Step 3 included testing and verifying the trained models using updated Google Earth image data sources to map the coastline and shoreline changes once the model had been built with high accuracy.

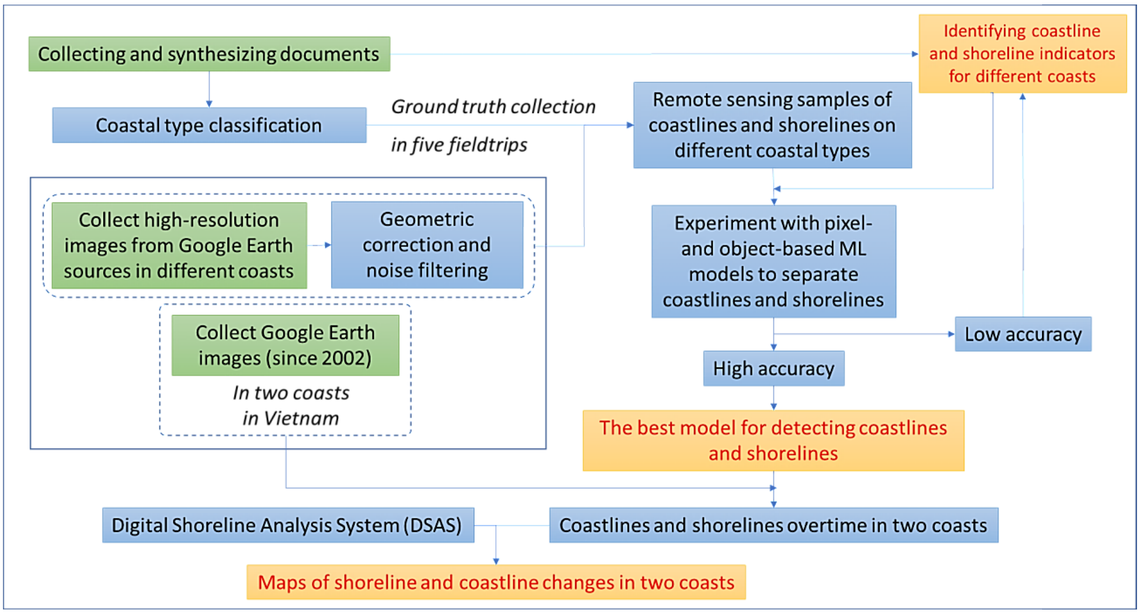

Figure 1. Structure diagram to develop ML model for mapping coastline and shoreline changes

2.1.1. Coastline and shoreline indicators

Scientists often encounter several challenges when identifying shorelines on the fields and in the satellite images, particularly when these image sources have not been supported frequently (Pollard et al., 2020;

Vinchon et al., 2006). In contrast to the more stable nature of coasts, shorelines are only there temporarily. Therefore, in wetland research, shorelines could be sampled 10 times per second, while certain studies looking at coastline changes require 10 to 20 years of sampling (Hanh and Furukawa, 2007).

The indicators for shorelines and coastlines could differ and depend on coastal types, such as cliffs, estuaries, and sandy beaches (Dang et al., 2022a; Hanley et al., 2014). Dang et al. (2022a) proposed some coastal components that can be used to identify coastlines and shorelines. Three indicator categories were found, including (1) visible indicators, (2) indicators based on tidal data, and (3) technique-based indicators. Visible signs are characteristic coastal objects that can be observed clearly in nature (Boak and Turner, 2005; Gens, 2010). The wet/dry zone border or high tide line, depending on high, low, and mean sea levels in a particular day or season, are example of the second indication type (Phan et al., 2019). Although the second indicator group is the least subjective of the groups mentioned above, this one has limitations when it is impossible to ascertain historical shorelines. Coastal signs observed in aerial and satellite images help identify coastline and shoreline at large scales (Gens, 2010; Stockdon et al., 2009). Despite having less accuracy than the two first indicator groups, the third one has become more prevalent in detecting shorelines and coastlines because its outcomes can be used for land use planning and natural hazard warming for long coasts. It improves the subjectivity of visible indicators and the lack of updates when using the tidal-datum-based indicators on the fields (Boak and Turner, 2005).

Depending on the tidal, land use/cover, and current ocean characteristics at a particular period, shoreline and coastline indicators may be detected alternatively in different coastal types (Boak and Turner, 2005). 13 indicators were chosen to identify coastlines and shorelines in sandy coasts from the 16 indicators listed by Dang et al. (2022a) (Fig. 2). Accordingly, the coastlines can be identified at three field locations, including points C1, C2, and C3. They are vegetation boundaries that have grown steadily on embryo- and fore-dunes or the boundaries of waves/storms' effects on land. Whereas the location of the shoreline is also significantly influenced by seasonal characteristics (Sowmya et al., 2019). There are two categories of shoreline indicators. The first category is connected to a specific physical characteristic, such as erosion and accretion signs along coasts (points C3 and C4 in Fig. 2). The second category relates to tide, wave, and river movement activities, such as high or low ocean current levels (from points S1 to S9). In the first category, owing to the effect of waves, tides, or wind during a brief time, a coastline displacement of 15 to 20 meters may be seen on a beach with a modest slope (Dang et al., 2020a; Phan et al., 2019). It alters the coast's geometry, affecting how waves behave near and on the coastline. Several nations have utilized the mean sea-level tides (S7, S8, and S9) as a criterion for identifying the shoreline and supporting coastal aquaculture and seafood businesses (Pajak and Leatherman, 2002). The second category is observed in the long-term trend and used to assess coastline modification due to extreme weather events like storms and cyclones, as well as new constructions of all living things and artificial structures, such as the existence of embankment constructions.

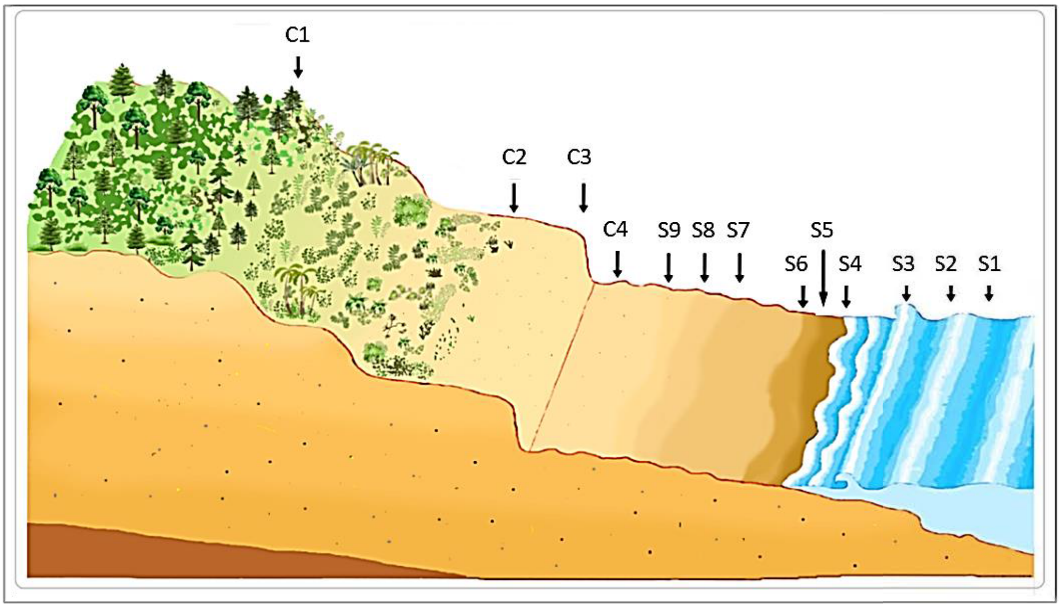

Coastline indicator

C1: Seaward stable dune vegetation line
C2: Seaward dune vegetation line
C3: Erosion scarp
C4: Storm/debris line

Shoreline indicator

S9: An old high tide water level
S8: Previous high tide high water level
S7: Mean high water (datum referenced)
S6: Wet/dry line or runup maxima
S5: Ground water exit point
S4: Instantaneous water line
S3: Shore-break maximum intensity
S2: Mean lower low water line (datum referenced)
S1: Beach toe/ crest of beach step

Figure 2. Indicators and their location to identify a coastline and a shoreline in sandy coasts

2.1.2. Input data preparation

Three procedures were taken to prepare the input sample. The Google Earth (GEE) database with a resolution of 0.7 m was directly downloaded from the Google Earth Pro (GEP) program in the first step to identify the coastline and shorelines precisely. These images frequently have various brightness levels (Dong et al., 2019; Tong et al., 2020). Therefore, for the computer to comprehend the pattern and diversity in the visual data requires many samples. To maximize the samples offered by Google Earth Pro software over different years, the image is saved in small areas in *.JPG format with a resolution of 4800×2800. The chosen appropriate scale was set to 1:500. After all background data from the software was removed during the image-saving process, the output images were collected with RGB colors. Seven provinces in the Center part of Vietnam were chosen to collect samples, including Quang Binh, Quang Tri, Hue, Da Nang, Quang Nam, Quang Ngai, and Binh Dinh (Fig. 3). The total length of the coasts exceeds 400 kilometers. 2010 through 2021 is the time frame for the image collection. The focus area is roughly 2 kilometers from the inland to the coast and 2 kilometers from the coast to the open ocean.

In step 2, coastal and shoreline digitization was done on 25,034 image frames obtained from step 1. To create a continuous image, the images taken in the same year and close to one another underwent a similar process. Due to the effects of spatial distortions on the high-resolution image produced by GEP software (Hu et al., 2013), a meticulous geometric correction has been carried out by keeping an eye out for fixed features like roads or other civil engineering constructions. The street-view data on ArcGIS software was used to fix the geometry features in this study.

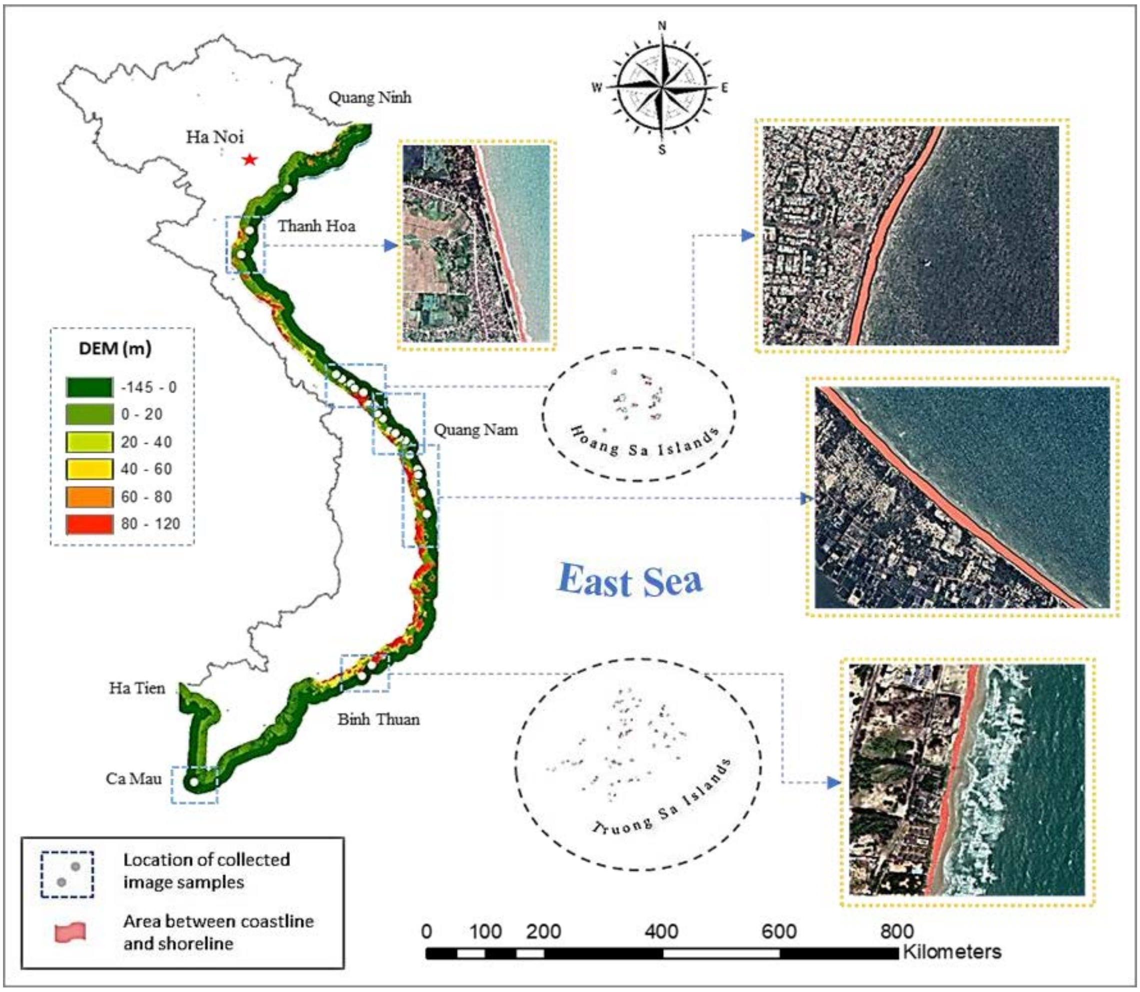

Figure 3. Places of high-resolution satellite-image samples chosen along Vietnam's coasts

Following the completion of the image data, the third step of editing the interpretative sample data involves digitizing the coastline and shorelines following the indicator described in Section 2.1.1. From 2017 to 2020, the author made four field excursions along Vietnam's coast, according to the shoreline and coastal indicators. Four fieldwork trips were conducted as part of the digitization process to (1) locate the coastline and shoreline in the field and compare them to conclusions drawn from the visual image interpretation from Google Earth sources; (2) measure and calculate the distance between the coastlines and shorelines on the fields; and (3) pinpoint areas with recent accretion and erosion phenomena. The "Discussion" section will go into detail on this subject. After this step, the surrounding areas have a value of "0" and the region between the coastlines and shorelines has a value of "1". The complete database was loaded into ML models after the GGE image and mask data were finished. The computer analyzes and learns the characteristics of the coastal region between beaches, shorelines, coastlines, and neighboring places.

2.2. Architecture of pixel-based models

2.2.1. Support Vector Machines

One of the most popular kernel-based learning algorithms is the Support Vector Machines technique, initially developed by Vapnik and his team in the late 1970s and notably useful for image classification (Karatzoglou et al., 2006). SVM is a linear binary classifier that distinguishes only one border between two classes, particularly between the region from coastlines to shorelines and the surrounding areas in this study, in its most basic configuration. For the linear SVM to work, the multidimensional data must be assumed to be linearly separable in the input (Pham et al., 2018; Xue Su et al., 2017). Specifically, SVMs use the training images obtained from Google Earth sources to find an ideal hyperplane (in the simplest example, a line) to divide the dataset into two specified classes. SVMs employ a subset of the training sample closest in the feature space to the ideal decision boundary, serving as support vectors, to maximize the separation or margin (Cervantes et al., 2020). It is possible to determine mathematically and geometrically the ideal hyperplane or maximum margin. It alludes to a decision boundary designed to reduce misclassification mistakes during training.

The kernel coefficient "gamma" and error term penalty parameter "C" were found and improved to optimize SVM models (Karatzoglou et al., 2006). Gamma increases may make the hyperplane smoother, and the training dataset fits SVM models. Even minimizing inaccuracies may cause overfitting. Thus, linear, polynomial, sigmoid, and radial basis (RBF) kernel functions impact SVM model performance (Hassan and Sadek, 2017). In the SVM development process in this study, "C" restricts training data. Thus, "gamma" and "C" were evaluated to maximize OA and kappa. The ideal "gamma" and "C" values were 0.35 and 90, respectively, in the classification of coastal and non-coastal regions. The best hyperplane is identified when the separation margin between coastal and non-coastal samples is most significant. The learning process is the iterative process of building a classifier with an optimal decision boundary.

2.2.2. Random Forests

The random forest classifier is made up of different tree classifiers, each of which is created using a random vector sampled separately from the coastal input data. Each tree then casts one unit of the vote for the most prevalent class to categorize the input data (Berhane et al., 2018; Piragnolo et al., 2017). This procedure reduces overfitting because the dataset was classified several times based on a random subset of training pixels, and each tree did not take all the training datasets to develop (Tian et al., 2016). Moreover, a random process is used to optimize the choice at each node. Finally, each tree casts a vote to determine the outcome, and the class that the majority of trees choose is the random forest's output.

In this study, two user-defined parameters are necessary to create a random forest classifier, including (i) the depth of each tree in the forest- or other words, for the number of rules each decision tree is permitted to develop. and (ii) the number of trees to be developed. In this study, the forest grew 50-trees classifiers, with the maximum depth of each tree being 30. By projecting the training data onto a randomly selected subspace and fitting each tree, the variety among the trees

(50 trees) is introduced, and each tree is developed with 30 rules. The majority of vote decided the output result.

2.3. Architecture of object-based models

2.3.1. Model layers

In the development of robotic fields, various structures, and methodologies are used in ML models (Alom et al., 2019; Nguyen et al., 2022b). To train a model for categorizing coastlines and shorelines, two ML architectures were created and examined in this part. Three dimensions width, length, and depth are present in its neurons. The depth parameter of input images is determined by spectral bands employed for prediction. Two different sizes of sub-images were explored, including 256×256×3 and 512×512×3, to determine the ideal size for training data (width, height, and depth, respectively). Models using smaller sub-images can recognize minor object features such as embryo dunes or vegetation (Dang et al., 2022b; H. N. Pham et al., 2022), whereas models using larger sub-images can recognize major object characteristics from the area between coastlines and shorelines, such as the bright color, continuous and linear distribution.

The DL architecture for image classification typically consists of six different layer types: (1) input, (2) convolutional (CONV), (3) batch normalization, (4) pooling, (5) concatenate, and (6) dropout layers. The training model analyzes all sub-images from the INPUT layer's raw pixel values (Albawi et al., 2018; Dang et al., 2020b). Filters in the CONV layers control the outputs of neurons. The Batch Normalization layer is used to simplify data to a new scale once all of the CONV layers have been trained. Internal covariate shift problems, or initial value changes during training, are minimized using this layer (Diakogiannis et al., 2020; Hatamizadeh et al., 2020). The standard deviation of each input layer depends on the mean and variance of the current batch, as follows:

$$p_i = \alpha\widehat{q_\iota} + \beta \tag{1}$$

In which the α and β are training parameters, $\widehat{q_\iota}$ is calculated based on mean (μ_A) and variance (σ_B^2) of mini-batch A = {q_1…q_m} based on following formulas:

$$\mu_A \leftarrow \frac{1}{m}\sum_{i=1}^{m} x_i \tag{2}$$

$$\sigma_A^2 = \frac{1}{m}\sum_{i=1}^{m}(q_i - \mu_A)^2 \tag{3}$$

$$\widehat{q_\iota} \leftarrow \frac{q_i - \mu_A}{\sqrt{\sigma_A^2 + \varepsilon}} \tag{4}$$

Regarding POOL layers, they use a 2×2 spatial matrix generated from activation functions to downscale data. This process removes poor sub-data from the input dataset. In contrast, a "ConvTrans" convolution matrix is generated at another site to up-sample a larger matrix before providing the outcome prediction (Heidler et al., 2022). Both matrix types have been used together in an expanding route and a contracting path, respectively, and linked by the concatenate layer. The data from earlier layers were condensed in the contracting route and combined with those from earlier layers in the extended path (Dang et al., 2022a). The Dropout layer is integrated with the Concatenate layers by deactivating extraneous neurons rather than training them. It plays an essential role in minimizing the cases of under and over-fitting and training mistakes. The ML models developed for this work employed a dropout value near 1.0 to maintain layer input visibility.

Various neural network architectures have been developed depending on the number and structures of the above six-layer types. It makes the performance of the ML models for shoreline and coastline extraction vary. To extract the shoreline and coastline in this study, the authors proposed two cutting-edge structures: U-Net and U-net3+. Their architecture can be explained as follows:

2.3.2. U-Net

U-Net models were first used to separate medical and geological imaging data (Ronneberger et al., 2015). These models have two expanding and contracting channels. The contracting route on the left half of the U-Net models (yellow blocks in Fig. 4) is comparable to a convolutional neural network architecture. Algorithms for right-hand up-sampling (blue blocks in Fig. 4) convert prediction results to the size of the starting image. 20 CONV layers use 3×3 filters to transform raw data from sizes 512×512 to 8×8 in the contracting route and back to 512×512 in the expanding path.

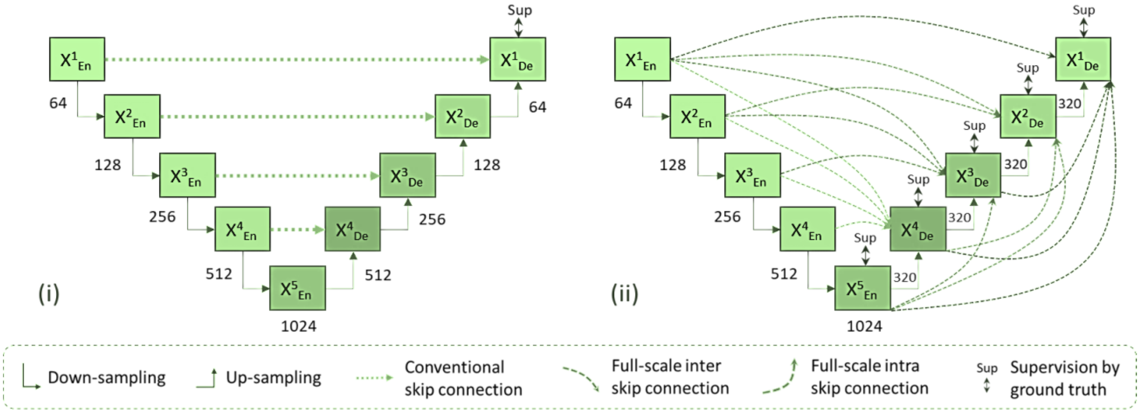

Figure 4. Architecture of U-Net (i) and U-Net3+ (ii) models used to train ML models for coastline and shoreline detection

In total, 256 filters were generated. The previous layer's width and height are doubled in the expanding path and reduced by half compared to the preceding layer in the contracting route (Fernández et al., 2020). On the right side, a conversion is made from intermediate values to the original image size. The 20 additional CONV layers are applied after batch normalization. The POOL layers are applied before the Dropout layers for the downscaling data process in the contracting route. For upscaling in expansive layers, transposed convolution matrices with Dropout layers are used. In total, 73-layer image processing algorithms were trained. The final products obtained from the Conv2D layer include two values: "one" represents the coastline and shoreline border, and "zero" represents other objects. Utilizing 73 layers (1×INPUT, 20×CONV, 4×Conv2DTrans, 4×POOL, 19×Batch-Normalization, 4×Concatenate, 19×Activation, and 2× Dropout) and 8041 sub-images, the trained U-Net interpreted the coastline and shoreline border. The input picture size and optimizer techniques allow for parameter adjustment of the CONV and Batch Normalization layers. The Adam optimizer was selected after testing the model's performance using other optimizer techniques, and the input picture size was varied between 256×256 and 512×512.

2.3.3. U-Net3+

As a novel U-shape-based architecture, the U-net3+ model uses the interconnection and the intra-connection between the encoder and the decoder to collect fine-grained information and coarse-grained semantics from the input dataset (Huang et al., 2020) (Fig. 4). Moreover, each side's output is coupled with a hybrid loss function. While U-net uses conventional skip connections, the U-net3+ structure includes full-scale skip connections between the encoder and decoder in complete scales but with fewer parameters to use the multi-scale features fully. Moreover, full-scale deep supervision is utilized in the UNet 3+ to train hierarchical representations from full-scale aggregated feature maps (Dang et al., 2022a). To seamlessly combine geographical information, 320 filters made in batch normalization and ReLU activation functions were applied to the feature maps. Each decoder level in the proposed U-Net 3+ produces a side output that the ground truth data checks. Each decoder phase's final layer is input into a 3×3 convolution layer with sigmoid and bilinear up-sampling functions.

2.4. Assessing model performances

To prevent over- or underfitting, the data's correctness was examined while the ML models were being developed (Dai et al., 2020; Moore, 2001). The optimal model is chosen when the results fit the training and validation data labels. Total accuracy and loss function values are two metrics to evaluate the effectiveness of the outcome models (Le et al., 2022). First, the following formulas were used to calculate the accuracy of each training model:

$$\mathrm{ACC} = 2\mathrm{TP} + \mathrm{FP} + \mathrm{FN} \qquad (1)$$

TP and FP are real positive values, while TN and FN are valid negative values. ACC values were gathered every epoch during the training period to track the model's performance. The authors employed a trained model with one of the lowest loss functions and the highest ACC to enhance the identification of all coastlines and shorelines.

To minimize the Cost function (C) or Loss function (L), both of which are convex functions, ideal weights must be chosen (Yang et al., 2019). Weight, training images, and labeled output results substantially impact the loss function. By lowering the loss function, the adjusted weight values can also help increase the precision of the following training coastline predictions. Following this process, the average loss values were computed as follows once all training sub-image data sets had been entered:

$$\mathcal{J} = \frac{1}{n}\sum_{x=1}^{n}\mathcal{L}^{(x)} \qquad (2)$$

where L((x)) is the loss value for a training sub-image during the training process, and n is the volume of training data collected.

The computer setup affects all models' training duration and size. With the help of the computer ASUS-1603, 12th Gen Intel(R) i7-12700KF 3.6GHz, 32.0 GB RAM, and NVIDIA GeForce RTX 3070, eight models were trained. A total of 13 hours were spent training each model utilizing U-Net architectures. All deep learning models were created using the Keras API and Tensorflow (Gulli, 2017). Throughout the training, the testing and validation accuracy was recorded. The ML training method may be stopped if the coefficient converges. However, it is restricted to 500 loops (or epochs - iterations through the training data).

2.4. New coastline and shoreline interpretation

Any model for identifying a coastline or shoreline that has been trained can be used to analyze new data. The coastlines and shorelines in Da Nang city and Quang Nam province in the center part of Vietnam during the past 10 years were compared using the DSAS tool in ArcGIS. The best ML model was used to separate shorelines and coastlines from the multi-temporal GGE's images, after which they were put into the DSAS tool (Nazeer et al., 2020). GGE's image data was gathered and prepared as described in Section 2.1. Once the final model is finished, more training data or ground truth points are not required. The model also generates the final coastline and shoreline maps by converting the new GGE's images into the appropriate spatial matrices using the learned spatial matrices.

3. Results

3.1. ML Model Performance

There were ten trained models based on four model structures, pixel-based (Random Forest and SVM) and object-based (U-net and U-Net3+). Tables 1 and 2 show that, compared to pixel-based models, object-based models provide greater spatial and attribute details on the coastlines and shorelines. Pixel-based models only provide details on individual pixels. These eight models make the trained models understand the differences between land, ocean, and the space between them and can be seen clearly in the networks trained based on U-net and U-Net3+ algorithms. In contrast, Random Forest and SVM models have low Kappa indices (0.86 and 0.88) and low overall accuracy (about 94%). The pixel-based ML models had a 3-6% chance of correctly predicting, and the error of omission in the non-coast zone is about 3.5%. The false favorable rates of pixel-based models in coastal areas were higher than in non-coast areas, 3% with the RF model and 1% with the SVM model. Four U-shaped models have a Kappa index and overall accuracy of more than 0.95 and 0.97.

Table 1. Accuracy values of two trained pixel-based ML models

Accuracy values	Random forest		SVM	
	Coast	Non-coast	Coast	Non-coast
Error of omission	3.4	10.0	5.2	6.1
Error of commission	9.4	3.6	6.1	5.2
Producer accuracy	96.6	90.0	94.8	93.9
User Accuracy	90.6	96.4	93.9	94.8
Kappa	0.86		0.88	
Overall Accuracy	93.3		94.3	

Table 2. Accuracy values of eight trained object-based ML models

Accuracy values	U-Net 256		U-Net 512		U-Net3+ 256		U-Net3+ 512	
	Coast	Non-coast	Coast	Non-coast	Coast	Non-coast	Coast	Non-coast
Error of omission	2.4	6.1	0.4	2.6	1.4	4.1	2.9	9.1
Error of commission	5.9	2.5	2.5	0.4	4.0	1.4	8.6	3.1
Producer accuracy	97.6	93.9	99.6	97.5	98.6	95.9	97.1	90.9
User Accuracy	94.1	97.5	97.4	99.6	96.0	98.6	91.4	96.9
Kappa	0.91		0.97		0.94		0.88	
Overall Accuracy	95.7		98.5		97.3		94.0	

Regarding object-based ML models, all U-Net-based structure models have accuracy values higher than 94%, especially the U-Net-256 model, which has an accuracy higher than 98%. U-net-shaped structures' false positives and negatives were recognized as lower than pixel-based models in both objects (coasts and non-coasts). However, the U-Net-3+ structure using the input cell size of 512×512 provides outcomes with low accuracy, which is equal to the pixel-based models. In addition to having the most petite model sizes, the prediction time of U-net3+ is longer than other models because of its more complex structure. Two U-Net models had the best accuracies while having middling training times and file sizes (about 13 hours and 118 MB). It demonstrates that the U-Net structure may be taught more quickly and efficiently compared to other network architectures.

3.2. The best model for coastline and shoreline extraction

For comparison, two DL models with accuracy more significant than 97% were used. Each U-net model was trained for 500 epochs in more than 13 hours. The loss function and accuracy values were perfectly convergent (Fig. 5). At the same time, the U-Net3+ model changed erratically after

50 epochs and 100,000 steps over 30 hours. The numbers have fallen since the 45th epoch. According to the validation accuracy and loss data, the model started overfitting during training but converged around the 40th epoch. In contrast, the time to train and predict pixel-based models was shorter than U-shaped models, and the accuracies were lower.

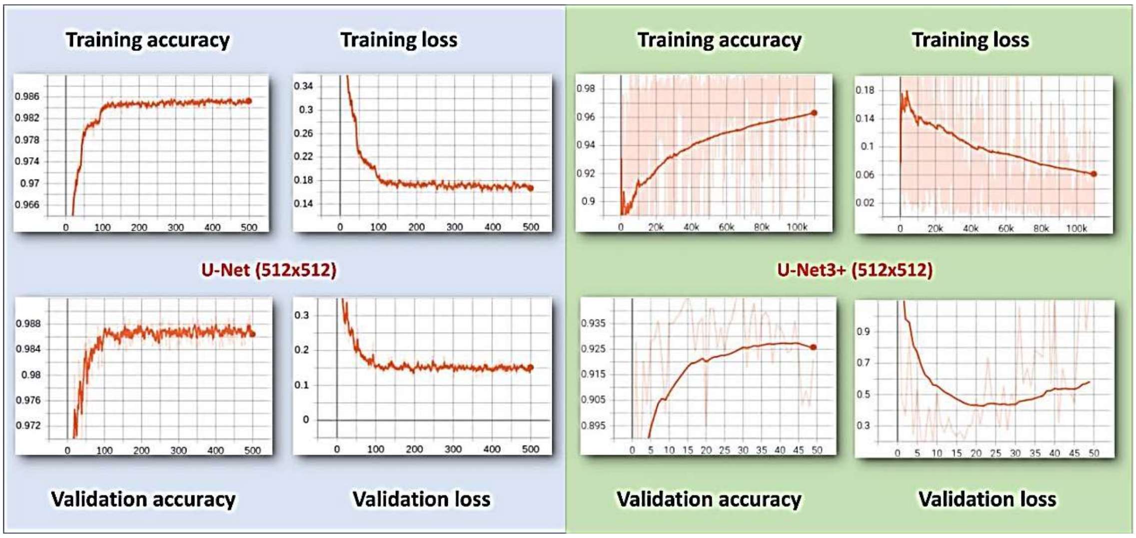

Figure 5. Diagrams show the accuracy and loss function fluctuation during training time of the best three ML models

Four trained models were used to evaluate four new images, as shown in Fig. 6. The regions between coastlines and shorelines are combined with urban regions in inland areas, such as white houses or bare land, in the forecast findings from the random forest and SVM models, particularly in the results of the Random Forest models. It is clear that both U-net-shaped models correctly comprehend the area between two lines. They may divide the area with low-growing vegetation that looks blurry in the images from the foredunes. However, the U-Net3+'s results still mixed a bit between the regions on the coasts and the sandy regions in the inland areas. The U-net model's outcomes are the best when they have the fewest mistakes. As a result, it was decided to forecast coastlines and shorelines along Vietnam's Center part in the following section.

3.3 Application of ML models for coastline/shoreline change assessments

The shoreline and coastline changes in the northern path of Quang Nam province, Da Nang City, and the estuary of Lai Giang River (in Binh Dinh province) were successfully retrieved from 2002 to 2021 based on the 512×512-U-Net model and DSAS tool (Fig. 7). Consequently, the space between the shoreline and the coastline reaches 30 to 40 m in the study area. This distance is closer to the Son Tra Peninsula (about 2-5 m). Based on the features of the study area's erosion and accretion during the last 20 years, the targeted coast was divided into 1922 coastal sections. The zones of erosion and accretion were divided into seven levels, five of which were associated with erosion (negative), one with accretion (positive), and one with relative stability.

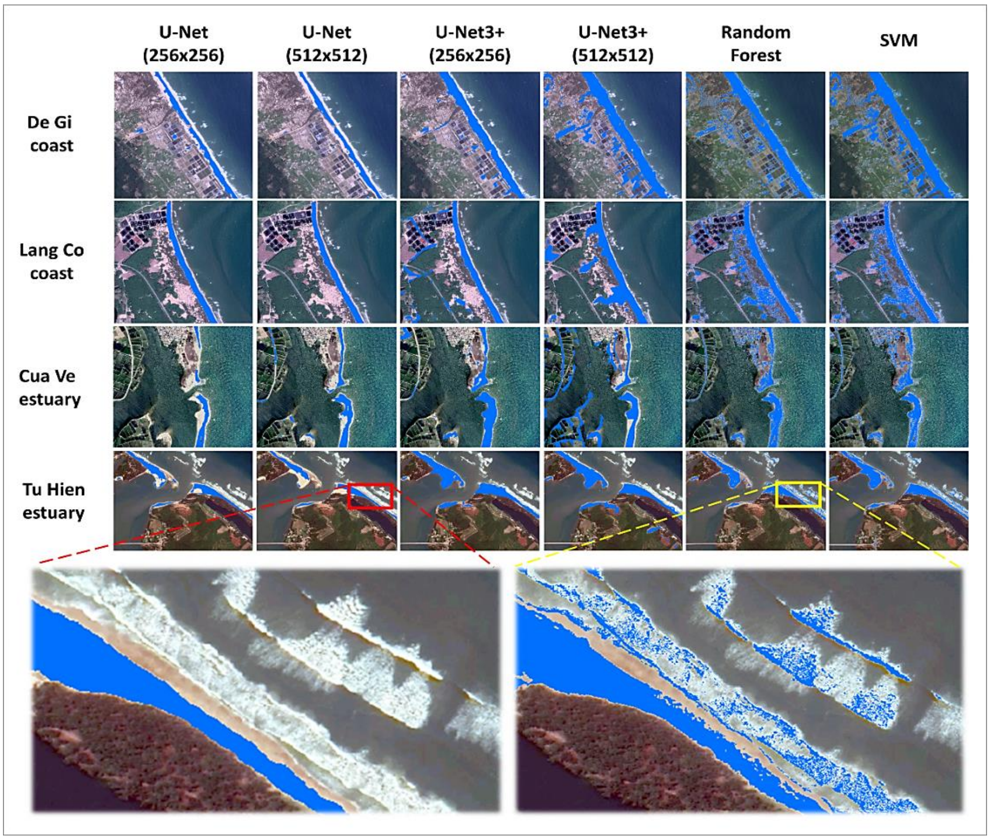

Figure 6. Four regions between the coastline and shoreline were interpreted based on the six ML models

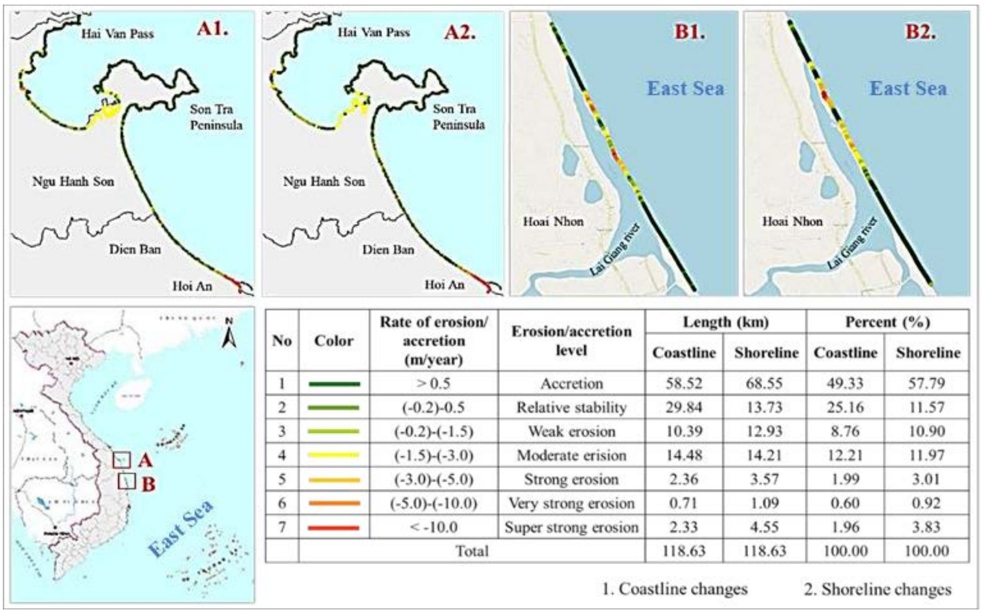

No	Color	Rate of erosion/ accretion (m/year)	Erosion/accretion level	Length (km)		Percent (%)	
				Coastline	Shoreline	Coastline	Shoreline
1	🟩	> 0.5	Accretion	58.52	68.55	49.33	57.79
2	🟩	(-0.2)-0.5	Relative stability	29.84	13.73	25.16	11.57
3	🟩	(-0.2)-(-1.5)	Weak erosion	10.39	12.93	8.76	10.90
4	🟨	(-1.5)-(-3.0)	Moderate erision	14.48	14.21	12.21	11.97
5	🟨	(-3.0)-(-5.0)	Strong erosion	2.36	3.57	1.99	3.01
6	🟧	(-5.0)-(-10.0)	Very strong erosion	0.71	1.09	0.60	0.92
7	🟥	< -10.0	Super strong erosion	2.33	4.55	1.96	3.83
	Total			118.63	118.63	100.00	100.00

1. Coastline changes 2. Shoreline changes

Figure 7. Rate of erosion and accretion in two case study areas in the Center path of Vietnam

However, the coasts remained steady throughout the study areas, while the shoreline changes were more apparent. While some shorelines reported an erosion process, others, including those in Lien Chieu district (Da Nang City) and Hoi An district (Quang Nam province), observed an accretion trend in Dien Ban district (Quang Nam province). The two most extensive estuaries, the Cua Dai and Nam O estuaries, show the most noticeable disparities. Between 2002 and 2021, the coastline in the Cua Dai area and Hoi An City suffered substantial degradation of more than 100 m. In the meantime, Fig. 7's green hue depicts several beaches along the accretion process in Hoi An's northern regions. On these coasts, eroding coastlines have been generated due to the land uses of the traditional settlements being modified for tourist development. Due to the influences of river and ocean currents, erosion is also seen in the southern path of the Cua Dai estuary in both coastline and shoreline-change predictions.

4. Discussions

4.1. Remote sensing data for coastline and shoreline classification

This study used high-resolution remote sensing images to locate 13 shorelines and coastlines for ML model input. Early coastline and shoreline identification studies focused on separating the land from the sea using mid-range resolution images (Boak and Turner, 2005; Yadav et al., 2017). Shoreline and coastline analysis was not based on Landsat images with 30 m resolution (Kumar et al., 2020). Sentinel images can only distinguish the coastline and shoreline from beach objects with 10m precision (Veettil et al., 2020). Fieldwork showed a 5-20 meter distance between the shoreline and the coastline. Sentinel-2 medium-range remote sensing images cannot detect this distance. Seaside residents said that only homes built without casuarina trees might be affected by sea level rise during storms. Coastal erosion has not affected most people who live 50-200 meters behind casuarina trees for generations. Thus, Landsat or Sentinel images alone cannot determine coastline and shoreline changes, significantly when storms raise sea levels and cause coastal erosion. High-resolution GGE image data with 0.7 m accuracy may aid real-time shoreline and coast separation research.

According to traditional studies, shorelines and coastlines require expert identification. Coastal managers find shoreline assessment difficult. Figure 2 shows how shorelines and coastlines are sampled differently. Shorelines were the wettest terrain around beaches. GGE images show the day's highest tidal limit.

Meanwhile, coastlines were more complicated than shorelines. Their furthest limit defines the coastlines where casuarina trees were planted to protect locals and tourists (Dang et al., 2021; Doody, 2005). The outermost boundary of stable vegetation on the image must define the coastline on sandy coasts. Ipomoea pes-caprae grows low on foredune sand beaches. Sometimes, this ecosystem is sparse. It grows on foredunes in fields outside of coastal casuarina forests. This ecosystem slowly invades the sea on accretion coastlines. Eroded coasts often eliminate this ecosystem. The beach sometimes extends far into the Casuarina forest.

Even high-resolution satellite images blur this ecosystem. Visual recognition was difficult for model input samples. This environment typically ranges from 10-20 m, 1-2 pixels on mid-range remote sensing images. Mid-range remote sensing data like Landsat or MODIS images can identify the Ipomoea pes-caprae ecosystem, extending up to 100-200 m, except along stable and high-accretion coastlines. GEP's high-resolution data may solve this problem. High-resolution data shows a transparent blue banded structure between the beach and coastal casuarina woods. Based on this structure, deep learning algorithms can locate coasts. The pixel-based models cannot resolve this problem because they do not have the spatial information to identify it. Then the pixel-based models misrepresented shoreline and coastline when there was the texture or reflectance of similar objects like bare land or white houses.

Shoreline changes affect coastal administration, planning, and development. Erosion destroys beach space, which is vital to tourism. Beach erosion destroys the permanently stable ground. It could affect coastal land management and people's lives. Thus, long-term protective construction should use coastal erosion or change to detect storm-related sea-level rise. According to local interviews, no significant changes have been observed in the past several decades besides urban growth-induced coastal changes. Thus, shoreline erosion or abrasion research is inaccurate. However, tides and satellite image acquisition do not affect coastline erosion or abrasion evaluation. Instead of shorelines, coastlines may benefit coastal management and planning.

This study used the 512x512-U-Net model to detect and evaluate coastline and shoreline changes in some case studies in the Center path of Vietnam. Van et al. found similar coastline and shoreline changes in Da Nang and Quang Nam (2013). Cham et al. (2020) report a 0.62-16.27 meter tidal adaptation variation along the Cua Dai coastline (particularly in the southern path of the research area A - Fig. 7). The results from the UNet model also showed significant erosion in the south (near Cua Dai with about 9-10 m/year), moderate erosion in the middle, and a steady coastline in the north. Significant coastline changes can be observed in some estuaries, such as Thu Bon, Cu De, and Lai Giang estuaries. Some regions under the impacts of human-made constructions, such as Da Nang Bay, along the Nguyen Tat Thanh Road, make it difficult for the ML models to detect coastlines and shorelines. High-resolution remote sensing images may track coastline and shoreline changes in the future. Google Earth multi-temporal remote sensing images showed 30 shorelines from 2002 to 2019. Spatial accuracy was 0.6m in this study. Better remote sensing photos like Worldview 2, 3, or UAVs can improve spatial precision to 0.3 m. It should be updated to the ML model in the future.

4.2. Models' comparison

In general, shorelines and coasts were identified using four suggested model structures. It is simple to translate the results from the other algorithms into shorelines and coasts in a regional manner. The shorelines are the lines closest to the offshore area, while the coastlines are the lines closest to the mainland. It supports evaluating coastal change by aiding in the precise and rapid dissection of shorelines and coastlines (Boak and Turner, 2005). When examined in further depth, several other fundamental disparities between the object-based and pixel-based findings became apparent. For linear groups, including coastlines and shorelines, the object-based models' predictions often coincided better with label data than pixel-based models. The results show how superior the U-shaped architecture findings are. The pixel-based technique does not consider spatial context, so they had more 'salt-and-pepper" signals and noise. These findings demonstrate object-based architectures' potential to enhance current coasts and could successfully resolve regions that could not be converted into label data.

Compared to the model using the U-Net structure, the model using the U-net3+ structure provides quite detailed output results. Consequently, the supplementary secondary information helped clarify the core information. The line between primary and secondary data is blurred because the weights applied in the following phases are fixed. Consequently, there is a general loss of information when decoding. This problem demonstrated that, even though artificial intelligence models employing U-net3+ networks can scan databases more thoroughly, it is not appropriate to use them to identify coastlines and shorelines. These models should be used to distinguish objects on photos with high multispectral resolution (above 1024×1024) or more excellent resolution. However, a mighty processing machine will be needed to employ these models.

5. Conclusions

To sum up, 13 indicators were suggested and utilized in this research to pinpoint Vietnam's coastlines and shorelines. As a result, the computer can learn to recognize these two items on high-resolution satellite images reliably and quickly. Based on trained weights in ML models, the computer chose appropriate indicators to distinguish the border between coastlines and shorelines for sandy coasts. With an image input size of 512×512, the fundamental U-Net appropriately comprehends the coastlines and shorelines among the four suggested pixel- and object-based structures. This model's accuracy is at its highest-ever level, 98%.

The evaluation of coastline and shoreline changes in coastal regions of Vietnam was done successfully using the best U-Net model. In the studied areas of Danang and Quang Nam, the DSAS tool revealed that land use changes in traditional villages for tourism are eroding these coastlines. According to predictions of coastline and littoral change, river and ocean currents erode the southern Cua Dai estuary. Therefore, it is fair to consider the coastline for evaluating coastal erosion brought on by the influence of sea level rise during storms. At the same time, the shoreline is helpful throughout the year for measuring tidal changes or the quick motions of current waves.

References

Albawi S., Mohammed T.A., Al-Zawi S., 2018. Understanding of a convolutional neural network. Proc. 2017 Int. Conf. Eng. Technol. ICET 2017 2018-Janua, 1-6. https://doi.org/10.1109/ICEngTechnol.2017.8308186.

Alom M.Z., Taha T.M., Yakopcic C., Westberg S., Sidike P., Nasrin M.S., Hasan M., Van Essen B.C., Awwal A.A.S., Asari, V.K., 2019. A state-of-the-art survey on deep learning theory and architectures. Electron., 8, 1-67. https://doi.org/10.3390/electronics8030292.

Berhane T.M., Lane C.R., Wu Q., Autrey B.C., Anenkhonov O.A., Chepinoga V.V., Liu H., 2018. Decision-tree, rule-based, and random forest classification of high-resolution multispectral imagery for wetland mapping and inventory. Remote Sens., 10(4), 580. https://doi.org/10.3390/rs10040580.

Boak E.H., Turner I.L., 2005. Shoreline Definition and Detection: A Review. J. Coast. Res., 214, 688-703. https://doi.org/10.2112/03-0071.1.

Cervantes J., Garcia-Lamont F., Rodríguez-Mazahua L. Lopez A., 2020. A comprehensive survey on support vector machine classification: Applications, challenges and trends. Neurocomputing, 408, 189-215.

Cham D.D., Nguyen H.S., Nguyen K.A., 2020. Coastal Vulnerability Assessments due to climate change in coastal sand-bar in Quang Binh, Quang Tri, Thua Thien Hue to propose sustainable likelihood. Science and Technics Publishing House, Hanoi, 364p.

Dai M., Leng X., Xiong B., Ji K., 2020. Sea-land segmentation method for SAR images based on improved BiSeNet. J. Radars, 9, 886-897. https://doi.org/10.12000/JR20089.

Dang K.B., Dang V.B., Bui Q.T., Nguyen V.V., Pham T.P.N., Ngo V.L., 2020a. A Convolutional Neural Network for Coastal Classification Based on ALOS and NOAA Satellite Data. IEEE Access, 8, 11824-11839. https://doi.org/10.1109/ACCESS.2020.2965231.

Dang K.B., Dang V.B., Ngo V.L., Vu K.C., Nguyen H., Nguyen D.A., Nguyen T.D.L., Pham T.P.N., Giang T.L., Nguyen H.D., Hieu Do T., 2022a. Application of deep learning models to detect coastlines and shorelines. J. Environ. Manage, 320, 115732. https://doi.org/10.1016/j.jenvman.2022.115732.

Dang K.B., Ha T., Nguyen T., Nguyen H.D., Truong Q.H., Vu T.P., 2022b. U-shaped deep-learning models for island ecosystem type classification a case study in Con Dao Island of Vietnam. One Ecosyst, 7, 23. https://doi.org/10.3897/oneeco.7.e79160.

Dang K.B., Ngo C.C., Ngo V.L., Dang V.B., 2022c. Coastal Vulnerability Assessment in Son Tra - Cua Dai region. VNU J. Sci. Earth Environ. Sci., 38, 55-65. https://doi.org/10.25073/2588-1094/vnuees.4842.

Dang K.B., Nguyen M.H., Nguyen D.A., Phan T.T.H., Giang T.L., Pham H.H., Nguyen T.N., Van Tran T.T., Bui D.T., 2020b. Coastal wetland classification with deep u-net convolutional networks and sentinel-2 imagery: A case study at the Tien Yen estuary of Vietnam. Remote Sens., 12, 1-26. https://doi.org/10.3390/rs12193270.

Dang K.B., Nguyen T.T., Ngo H.H., Burkhard B., Müller F., Dang V.B., Nguyen H., Ngo V.L., Pham T.P.N., 2021. Integrated methods and scenarios for assessment of sand dunes ecosystem services. J. Environ. Manage, 289, 112485. https://doi.org/10.1016/j.jenvman.2021.112485.

Diakogiannis F.I., Waldner F., Caccetta P., Wu C., 2020. ResUNet-a: A deep learning framework for semantic segmentation of remotely sensed data. ISPRS J. Photogramm. Remote Sens., 162, 94-114. https://doi.org/10.1016/j.isprsjprs.2020.01.013.

Dong T., Shen Y., Zhang J., Ye Y., Fan J., 2019. Progressive cascaded convolutional neural networks for single tree detection with google earth imagery. Remote Sens, 11(15), 1786. https://doi.org/10.3390/rs11151786.

Doody J.P., 2005. Sand dune inventory of Europe. Proc. Dunes Estuaries Int. Conf. Nat. Restor. Pract. Eur. Coast. Habitats, 45-54.

Duong H.H., Ngo T.T.H., Tran V.P., Nguyen D.D., Avand M., Nguyen H.D., Amiri M., Van Le H., Prakash I., Binh Thai P., 2022. Development and application of hybrid artificial intelligence models for groundwater potential mapping and assessment. Vietnam Journal of Earth Sciences, 44(3), 410-429. https://doi.org/https://doi.org/10.15625/2615-9783/17240.

Escudero-Castillo M., Felix-Delgado A., Silva R., Mariño-Tapia I., Mendoza E., 2018. Beach erosion and loss of protection environmental services in Cancun, Mexico. Ocean Coast. Manag, 156, 183-197. https://doi.org/10.1016/j.ocecoaman.2017.06.015.

Fernández J.G., Abdellaoui I.A., Mehrkanoon S., 2020. Deep coastal sea elements forecasting using U-Net based models, 252, 27. 109445.

Gallina V., Torresan S., Zabeo A., Critto A., Glade T., Marcomini A., 2020. A multi-risk methodology for the assessment of climate change impacts in coastal zones. Sustain, 12(9), 3697. https://doi.org/10.3390/su12093697.

Gens R., 2010. Remote sensing of coastlines: detection, extraction and monitoring. Int. J. Remote Sens., 31, 1819-1836.

Gordana K., Avdan U., 2019. Evaluating Sentinel-2 Red-Edge Bands for Wetland Classification. Proceedings 18, 12. https://doi.org/10.3390/ecrs-3-06184.

Gulli A., 2017. Deep Learning with Keras - Implement neural networks with Keras on Theano and TensorFlow. Packt Publishing Ltd., Birmingham, UK, 318p.

Hanh P.T.T., Furukawa M., 2007. Impact of sea level rise on coastal zone of Vietnam. Bull. Coll. os Cience Univ. TGE Ryukyus, 84, 45-59.

Hanley M.E., Hoggart S.P.G.G., Simmonds D.J., Bichot A., Colangelo M.A., Bozzeda F., Heurtefeux H., Ondiviela B., Ostrowski R., Recio M., Trude R., Zawadzka-Kahlau E., Thompson R.C., 2014. Shifting sands? Coastal protection by sand banks, beaches and dunes. Coast. Eng., 87, 136-146. https://doi.org/10.1016/j.coastaleng.2013.10.020.

Hassan S.M., Sadek M.F., 2017. Geological mapping and spectral based classification of basement rocks using remote sensing data analysis: The Korbiai-Gerf nappe complex, South Eastern Desert, Egypt.

J. African Earth Sci., 134, 404-418. https://doi.org/10.1016/j.jafrearsci.2017.07.006

Hatamizadeh A., Terzopoulos D., Myronenko A., 2020. Edge-Gated CNNs for Volumetric Semantic Segmentation of Medical Images, 8-17. https://doi.org/10.1101/2020.03.14.992115.

Heidler K., Mou L., Baumhoer C., Dietz A., Zhu X.X., 2022. HED-UNet: Combined Segmentation and Edge Detection for Monitoring the Antarctic Coastline. IEEE Trans. Geosci. Remote Sens., 60, 1-13. https://doi.org/10.1109/TGRS.2021.3064606.

Hoang T.T.H., Dang K.B., Anton V.R., 2022. Comprehensive assessment of coastal tourism potential in Vietnam. Vietnam J. Earth Sci., 44, 535-558. https://doi.org/https://doi.org/10.15625/2615-9783/17374.

Hoang V.L., Nguyen Tien Thanh, Vu T.T., Nguyen Thanh Tung, Nguyen L.A., Dao B.D., Le V.D., Tran N.D., Nguyen H.H., 2021. Holocene sediementation offshore Southeast Vietnam based on geophysical interpretation and sediment composition analysis. Vietnam J. Earth Sci., 43(3), 336-379. https://doi.org/https://doi.org/10.15625/2615-9783/16268.

Hu Q., Wu W., Xia T., Yu Q., Yang P., Li Z., Song Q., 2013. Exploring the use of google earth imagery and object-based methods in land use/cover mapping. Remote Sens., 5, 6026-6042. https://doi.org/10.3390/rs5116026.

Huang H., Lin L., Tong R., Hu H., Zhang Q., Iwamoto Y., Han X., Chen Y.W., Wu J., 2020. UNet 3+: A Full-Scale Connected UNet for Medical Image Segmentation. ICASSP, IEEE Int. Conf. Acoust. Speech Signal Process. - Proc. 2020-May, 1055-1059. https://doi.org/10.1109/ICASSP40776.2020.9053405.

Karatzoglou A., Meyer D., Hornik K., 2006. Support Vector Algorithm in R. J. Stat. Softw., 15, 1-28.

Kumar L., Afzal M.S., Afzal M.M., 2020. Mapping shoreline change using machine learning: a case study from the eastern Indian coast. Acta Geophys., 68, 1127-1143. https://doi.org/10.1007/s11600-020-00454-9.

Le H.A., Nguyen T.A., Nguyen D.D., Prakash I., 2020. Prediction of soil unconfined compressive strength using Artificial Neural Network Model. Vietnam J. Earth Sci., 42(3), 255-264. https://doi.org/https://doi.org/10.15625/0866-7187/42/3/15342.

Le Q.T., Dang K.B., Giang T.L., Tong T.H.A., Nguyen V.G., Nguyen T.D.L., Yasir M., 2022. Deep learning model development for detecting coffee tree changes based on Sentinel-2 imagery in Vietnam. IEEE Access, 10, 109097-109107. https://doi.org/10.1109/ACCESS.2022.3203405.

Loi D.T., Khac D.V., Hung D.N., Dong N.T., Vinh D.X., Weber C., 2021. Monitoring of coastline change using Sentinel-2A and Landsat 8 data, a case study of Cam Pha city - Quang Ninh province. Vietnam J. Earth Sci., 43(3), 249-272. https://doi.org/https://doi.org/10.15625/2615-9783/16066.

Martínez C., Contreras-López M., Winckler P., Hidalgo H., Godoy E., Agredano R., 2018. Coastal erosion in central Chile: A new hazard? Ocean Coast. Manag., 156, 141-155. https://doi.org/10.1016/j.ocecoaman.2017.07.011.

Mineur F., Arenas F., Assis J., Davies A.J., Engelen A.H., Fernandes F., Malta E. Jan, Thibaut T., Van Nguyen T., Vaz-Pinto F., Vranken S., Serrão E.A., De Clerck O., 2015. European seaweeds under pressure: Consequences for communities and ecosystem functioning. J. Sea Res., 98, 91-108. https://doi.org/10.1016/j.seares.2014.11.004.

Moore A., 2001. Cross-validation for detecting and preventing overfitting. Sch. Comput. Sci. Carneigie Mellon, 1-27.

Nazeer M., Waqas M., Shahzad M.I., Zia I., Wu W., 2020. Coastline vulnerability assessment through landsat and cubesats in a coastal mega city. Remote Sens., 12, 1-24. https://doi.org/10.3390/rs12050749.

Nguyen C.N., Nguyen V.D., Ha T.G., Dinh Q. Van, Nguyen L.M., Huang B.-S., Pham T.T., Nguyen T.H., Le Q.K., Nguyen H.H., 2022a. Automatic earthquake detection and phase picking in Muong Te, Lai Chau region: an application of machine learning in observational seismology in Vietnam. Vietnam J. Earth Sci., 44(3), 430-446. https://doi.org/https://doi.org/10.15625/2615-9783/17253.

Nguyen D.T., Le T.T., Vuong A.T., Nguyen Q.V., 2020. Identify some aerodynamic parameters of a airplane using the spiking neural network.pdf. Vietnam J. Earth Sci., 42(3), 276-287. https://doi.org/https://doi.org/10.15625/0866-7187/42/3/15355.

Nguyen T.A., Ly H.B., Jaafari A., Pham T.B., 2020. Estimation of friction capacity of driven piles in clay using artificial Neural Network.pdf. Vietnam J. Earth Sci., 42(3), 265-275. https://doi.org/https://doi.org/10.15625/0866-7187/42/3/15182.

Nhu V.-H., Bui T.T., My L.N., Vuong H., Duc H.N., 2022. A new approach based on integration of random subspace and C4.5 decision tree learning method for spatial prediction of shallow landslides. Vietnam J. Earth Sci., 44(3), 327-342. https://doi.org/https://doi.org/10.15625/2615-9783/16929.

Nirmala B.J., Miriyala S., Ratnam D.V., Dutta G., 2022. Assessment of machine learning techniques for prediction of integrated water vapor using meteorological data. Vietnam J. Earth Sci., 44(4), 521-534. https://doi.org/https://doi.org/10.15625/2615-9783/17373.

Pajak M.J., Leatherman S., 2002. The high water line as shoreline indicator. J. Coast. Res., 18, 329-337.

Pham B.T., Prakash I., Khosravi K., Chapi K., Trinh P.T., Ngo T.Q., Hosseini S.V, Bui D.T., 2018. A comparison of Support Vector Machines and Bayesian algorithms for landslide susceptibility modelling. Geocarto Int., 123. https://doi.org/10.1080/10106049.2018.1489422.

Pham H.N., Dang K.B., Nguyen T.V., Tran N.C., Ngo X.Q., Nguyen D.A., Phan T.T.H., Nguyen T.T., Guo W., Ngo H.H., 2022. A new deep learning approach based on bilateral semantic segmentation models for sustainable estuarine wetland ecosystem management. Sci. Total Environ., 838, 155826. https://doi.org/10.1016/j.scitotenv.2022.155826.

Pham T.B., Nguyen D.D., Bui T.Q.A., Nguyen M.D., Vu T.T., Prakash I., 2022. Estimation of load-bearing capacity of bored piles using machine learning models. Vietnam J. Earth Sci., 44(4), 470-480. https://doi.org/https://doi.org/10.15625/2615-9783/17177.

Pham T.B., Singh S.K., Ly H.B., 2020. Using Artificial Neural Network (ANN) for prediction of soil coefficient of consolidation. Vietnam J. Earth Sci., 42, 311-319. https://doi.org/https://doi.org/10.15625/0866-7187/42/4/15008.

Phan H.M., Ye Q., Reniers A.J.H.M., Stive M.J.F., 2019. Tidal wave propagation along The Mekong deltaic coast. Estuar. Coast. Shelf Sci., 220, 73-98. https://doi.org/10.1016/j.ecss.2019.01.026.

Piragnolo M., Masiero A., Pirotti F., 2017. Comparison of Random Forest and Support Vector Machine classifiers using UAV remote sensing imagery. Geophys. Res. Abstr. EGU Gen. Assem., 19, 2017-15692.

Pollard E., Corns A., Henry S., Shaw R., 2020. Coastal Erosion and the Promontory Fort: Appearance and Use during Late Iron Age and Early Medieval County Waterford, Ireland. Sustainability, 12, 5794. https://doi.org/10.3390/su12145794.

Ronneberger O., Fischer P., Brox T., 2015. U-net: Convolutional networks for biomedical image segmentation. Lect. Notes Comput. Sci. (including Subser. Lect. Notes Artif. Intell. Lect. Notes Bioinformatics), 9351, 234-241. https://doi.org/10.1007/978-3-319-24574-4_28.

Sowmya K., Sri M.D., Bhaskar A.S., Jayappa K.S., 2019. Long-term coastal erosion assessment along the coast of Karnataka, west coast of India. Int. J. Sediment Res., 34, 335-344. https://doi.org/10.1016/j.ijsrc.2018.12.007.

Stockdon H.F., et al., 2009. Extraction of lidar- based dune-crest elevations for use in examining the vulner- ability of beaches to inundation during hurricanes. J. Coast. Res., 53, 59-65.

Tian S., Zhang X., Tian J., Sun Q., 2016. Random forest classification of wetland landcovers from multi-sensor data in the arid region of Xinjiang, China. Remote Sens., 8, 1-14. https://doi.org/10.3390/rs8110954.

Titus J.G., Richman C., 2001. Maps of lands vulnerble to sea level rise: Modeled elevations along the US Atlantic and Gulf coasts. Clim. Res., 18, 205-228. https://doi.org/10.3354/cr018205.

Tong X.Y., Xia G.S., Lu Q., Shen H., Li S., You S., Zhang L., 2020. Land-cover classification with high-resolution remote sensing images using transferable deep models. Remote Sens. Environ., 237, 111322. https://doi.org/10.1016/j.rse.2019.111322.

Toure S., Diop O., Kpalma K., Maiga A.S., 2019. Shoreline detection using optical remote sensing: A review. ISPRS Int. J. Geo-Information, 8(75), 21. https://doi.org/10.3390/ijgi8020075.

Tran V.Q., Prakash I., 2020. Prediction of soil loss due to erosion using support vector machine model. Vietnam J. Earth Sci., 42(3), 247-254. https://doi.org/https://doi.org/10.15625/0866-7187/42/3/15050.

Veettil B.K., Costi J., Marques W.C., Tran X.L., Quang N.X., Van D.D., Hoai P.N., 2020. Coastal environmental changes in Southeast Asia: A study from Quang Nam Province, Central Vietnam. Reg. Stud. Mar. Sci., 39, 101420. https://doi.org/10.1016/j.rsma.2020.101420.

Vinchon C., Idier D., Garcin M., Y. Balouin, Mallet C., Aubié S., Closset L., 2006. Response of the Coastline to Climate Change. Specific Report for the RESPONSE Project LIFE-Environment programm: Evolution of coastal risk (erosion and marine flooding) on the Aquitaine and Languedoc-Roussillon pilot regions. Final report. BRGM/RP-54718.

Vu V.P., Nguyen H., Hoang T.V., Nguyen B., Dao M.T., 2004. Some results of geomorphological research on the modern coast of Vietnam (in Vietnamese). VNU J. Sci. Earth Environ. Sci., 4, 73-81.

Xue Su Y., Xu H., Jiao Yan L., 2017. Support vector machine-based open crop model (SBOCM): Case of rice production in China. Saudi J. Biol. Sci., 24, 537-547. https://doi.org/10.1016/j.sjbs.2017.01.024.

Yadav A., Dodamani B.M., Dwarakish, 2017. Shoreline Change: A Review, in: Mangalore Institute of Technology & Engineering. Moodbidri. India, 5-10.

Yang W., Wang W., Zhang X., Sun S., Liao Q., 2019. Lightweight Feature Fusion Network for Single Image Super-Resolution. IEEE Signal Process. Lett., 26, 538-542. https://doi.org/10.1109/LSP.2018.2890770.